coatings

MDPI

Article

Epoxy-Based Superhydrophobic Coating Reinforced by Functional Polyaniline@Expanded Graphite with Multiple Anticorrosion Mechanisms

Meiling Li [1], Yuxin Fu [2], Chijia Wang [1], Yexiang Cui [1], Xiguang Zhang [1], Haiyan Li [1], Zhanjian Liu [2,*] and Huaiyuan Wang [2,3,4,*]

[1] College of Chemistry and Chemical Engineering, Northeast Petroleum University, Daqing 163318, China
[2] College of New Energy & Materials, Northeast Petroleum University, Daqing 163318, China
[3] School of Chemical Engineering and Technology, Tianjin University, Tianjin 300350, China
[4] State Key Laboratory of Chemical Engineering and Low-Carbon Technology, Tianjin University, Tianjin 300350, China
* Correspondence: liuzhanjian2012@163.com (Z.L.); hywang2007@163.com (H.W.)

Abstract

The anti-corrosion performance of epoxy coatings in saline solution environments is restricted by their surface hydrophilicity and microporous defects. Herein, we developed a modified epoxy (MEP)-based superhydrophobic anticorrosive coating by fluorinated resin matrix and incorporation of polyaniline@expanded graphite (FPANI@MEG) anticorrosive fillers. The FPANI@MEG fillers were fabricated via in situ polymerization of aniline on the surface of dopamine-modified expanded graphite to construct the micro-nano hierarchical structure required for superhydrophobicity, while providing barrier shielding and active passivation functions. The results showed that the final coating exhibited excellent superhydrophobicity with a water contact angle of 156.5 ± 1.8° and sliding angle of 3.0 ± 0.6°, along with excellent adhesion and adaptability to various complex environments. Meanwhile, the coating maintained superhydrophobicity after 400 cycles of Taber abrasion and 450 g of falling-sand impact, demonstrating hydrophobic robustness. Furthermore, the coating exhibited a low-frequency impedance modulus of 2.30×10^7 Ω·cm^2 after immersion in NaCl solution for 15 days. The synergistic combination of air film shielding, physical barrier, and active passivation endowed the coating with good anticorrosion performance. This work may provide a theoretical reference for improving the corrosion protection of epoxy-based superhydrophobic coatings on carbon steel in aggressive saline solution environments.

Keywords: superhydrophobic; anti-corrosion coatings; multiple anticorrosion; functional filler for anti-corrosion coatings; polyaniline; expanded graphite

Academic Editor: Kirill A. Emelyanenko

Received: 5 April 2026
Revised: 23 April 2026
Accepted: 4 May 2026
Published: 8 May 2026

1. Introduction

Carbon steel is widely used in marine engineering, chemical equipment and oil transport pipeline due to its reliable mechanical properties, ease of processing and cost-effectiveness [1–3]. However, influenced by its service environment and inherent characteristics, carbon steel is highly susceptible to electrochemical corrosion, especially in corrosive environments such as humid conditions [4,5], salt spray [6] and industrial atmospheres, which can lead to material failure, equipment damage, and even safety incidents [7]. Currently, the development of protective technologies such as corrosion inhibitors, electrochemical techniques, and coating applications has proven effective in slowing down

the rate of metal corrosion [8–10]. Among these, epoxy resin coatings have become a typical representative in coating protection systems due to their excellent adhesion, good chemical stability, and barrier properties [11,12]. However, epoxy resin coatings are prone to micropores and pinholes during curing and exhibit surface hydrophilicity due to their hydrophilic groups after film formation, which increases the possibility of adhesion and penetration of corrosive media (H_2O, O_2, Cl^-), ultimately resulting in accelerated failure of the coating [13]. Therefore, enhancing the surface hydrophobicity of coatings, reducing the adhesion of corrosive media to coating surfaces and prolonging their permeation pathways within coatings is of great significance for improving the anti-corrosion performance of epoxy-based coatings.

Inspired by the natural hydrophobicity of lotus leaves, superhydrophobic surfaces, defined as solid surfaces with a water contact angle greater than 150° and a sliding angle less than 10°, possess outstanding water-repellent performance, which can significantly reduce the contact area between coatings and corrosive liquids. The trapped air cushion can effectively retard the penetration and diffusion of corrosive media [14–17], demonstrating outstanding anticorrosion performance. In recent years, epoxy-based composite coatings with superhydrophobicity have made notable progress in the field of corrosion protection [18–22]. For instance, Yang et al. [21] prepared an epoxy superhydrophobic coating containing micron boron nitride and nano Al_2O_3 fillers on aluminum alloy substrates via simple spraying. The coating showed outstanding superhydrophobicity and anti-corrosion performance, with over 99% protection efficiency for the substrate in 3.5 wt% NaCl solution, attributed to the formation of an air cushion layer at the coating/solution interface, which significantly impeded the penetration of corrosive liquids and reduced the occurrence probability of substrate corrosion. Zhang et al. [22] developed a kaolin-based superhydrophobic coating using a layer-by-layer spray-coating method with epoxy resin as the binder. The coating demonstrated durable anti-corrosion performance, increasing the surface charge transfer resistance and low-frequency modulus by seven orders of magnitude. The enhanced protection was due to the air cushion trapped in its micro-nano hierarchical structure, which significantly reduced the solid–liquid contact area and limited the mobility of corrosive ions. However, the continuous air cushion barrier on the superhydrophobic coating surface is gradually infiltrated under sustained liquid pressure during prolonged immersion, leading to the eventual loss of superhydrophobicity. Therefore, further enhancing the barrier properties and active anticorrosion capability of superhydrophobic coatings is crucial for improving their corrosion protection performance.

Polyaniline (PANI) exhibits broad application prospects in the field of metal corrosion protection, owing to its unique redox characteristics and doping/dedoping behavior [23–25]. Its anticorrosion mechanism primarily lies in its ability to induce the formation of a dense passive film on the metal surface, achieving a transition from passive barrier to active passivation. Rahela et al. [26] revealed the active passivation mechanism of PANI films in corrosion protection of stainless steel. The study found that even in the presence of artificial pinhole defects in the PANI coating, the surrounding emeraldine salt form of PANI could stabilize the potential of the exposed stainless-steel region within the passivation range through electrochemical action, thereby achieving active self-healing of the defective area. Mourya et al. [27] fabricated reduced graphene oxide-polyaniline (rmGO-PANI-ES) nanocomposites as functional fillers for epoxy coatings, where PANI-ES grew on the active sites of rmGO and enwrapped its lamellar structure. The dual anticorrosion system, combining the physical barrier effect of rmGO and the passive film promoted by PANI-ES, exhibited remarkable corrosion protection compared to the pure epoxy coating. On the basis of the dual anticorrosion mechanism, introducing superhydrophobicity to the coating surface allows the establishment of a triple anticorrosion system. Nevertheless, most conventional two-dimensional lamellar barrier materials (like graphene, MXene, mica)

are difficult to directly construct the micro-nano hierarchical structures required for superhydrophobic surfaces. By comparison, expanded graphite (EG) features a distinctive worm-like three-dimensional lamellar stacking structure that simultaneously provides physical barrier performance and forms micro-nano rough structures conducive to superhydrophobicity [28], while being considerably more economical than conventional lamellar barriers.

In this work, a modified epoxy-based superhydrophobic anticorrosive coating with triple anticorrosion mechanisms was fabricated via a one-step spraying method. The hydrophobicity of the resin matrix was enhanced by chemically modifying the epoxy resin with a fluorosilane modifier. PANI nanoparticles were loaded onto the surface of micron-sized EG via in situ polymerization, enabling the filler to serve dual roles as a functional anticorrosive additive and a builder of the micro-nano hierarchical structure required for superhydrophobicity. Polydopamine was employed to bridge PANI and EG through π-π conjugation and hydrogen bonding, synergistically enhancing interfacial adhesion between components and structural stability of the composite filler. Meanwhile, the prepared coating achieved reinforced anticorrosion performance through the synergistic action of multiple anticorrosion mechanisms, including air film shielding, physical barrier, and active passivation. This work is expected to provide a reference for the development of coatings featuring a triple anticorrosion system.

2. Experimental

2.1. Materials

Epoxy resin E44 and curing agent 593 were obtained from Guangzhou Haihong Chemical Co., Ltd. (Guangzhou, China). Expandable graphite (EG, 800 mesh) was provided by Qingdao Yanhai Carbon Materials Co., Ltd. (Qingdao, China). Xylene (99%), absolute ethanol (≥99.7%), tris(hydroxymethyl)aminomethane (Tris), and phosphoric acid (H_3PO_4, AR) were purchased from Liaoning Quanrui Reagent Co., Ltd. (Jinzhou, China). 1H,1H,2H,2H-perfluorooctyltriethoxysilane (POTS, >97%), 1H,1H,2H,2H-tridecafluoro-n-octyltriethoxysilane (FAS, >97%), dopamine hydrochloride (≥99%), ammonium peroxydisulfate (APS, 98.5%), and aniline (AN, ≥99.5%) were purchased from Shanghai Macklin Biochemical Co., Ltd. (Shanghai, China). N-butanol (≥99.5%), sodium chloride (NaCl, ≥99.5%), hydrochloric acid (HCl, 36–38 wt%), and glacial acetic acid (≥99.5 wt%) were obtained from Tianjin Damao Chemical Reagent Co., Ltd. (Tianjin, China). Deionized water was made in the laboratory.

2.2. Substrate Pretreatment

Q235 carbon steel plates (60 mm × 60 mm × 1 mm) were used as coating substrates. Prior to spraying, the substrates were polished sequentially with 600, 800, 1000, and 2000-grit sandpapers to remove the surface oxide film. Subsequently, the substrates were ultrasonically cleaned with anhydrous ethanol to eliminate abrasive debris and grease, followed by drying in an oven at 80 °C for later use.

2.3. Synthesis of FPANI@MEG Particles

Tris-HCl buffer was prepared by adding 6.055 g of Tris to 800 mL of distilled water in a 1000 mL volumetric flask. After complete dissolution, the pH was adjusted to 8 by adding 1.2 mol L^{-1} hydrochloric acid, and the solution was diluted to 1000 mL.

EG was expanded at 550 °C for 2 h in a muffle furnace. After cooling to room temperature, 2 g of EG was dispersed in 200 mL of the above Tris-HCl buffer, followed by the addition of 0.12 g of dopamine hydrochloride. The mixture was magnetically stirred for 12 h to achieve sufficient polymerization of the dopamine on the EG surface. The product was then vacuum-filtered, washed with distilled water and anhydrous ethanol,

and freeze-dried for 12 h to obtain polydopamine (PDA)-modified EG, denoted as MEG. 5 mL of AN was added dropwise to 130 mL of 1 mol L^{-1} phosphoric acid solution under magnetic stirring. After 30 min of stirring, 2 g of MEG was added, and stirring continued for 30 min. Subsequently, 50 mL of 25 wt% APS solution was added dropwise, and the mixture was stirred for 3 h to enable in situ polymerization of AN on the MEG surface. The solution was vacuum-filtered, washed with distilled water, and freeze-dried to obtain PANI-loaded MEG, denoted as PANI@MEG.

Then, low-surface-energy substance POTS was employed to enhance the hydrophobicity of the filler. Specifically, 1 g of PANI@MEG was dispersed in 20 mL of anhydrous ethanol, followed by the addition of 200 µL of POTS. Appropriate amounts of distilled water and glacial acetic acid were also added to promote hydrolysis. After magnetic stirring for 12 h, the mixture was dried at 80 °C to yield fluorinated PANI@MEG, denoted as FPANI@MEG. The illustration for the preparation process for FPANI@MEG composite particles is shown in Figure 1a.

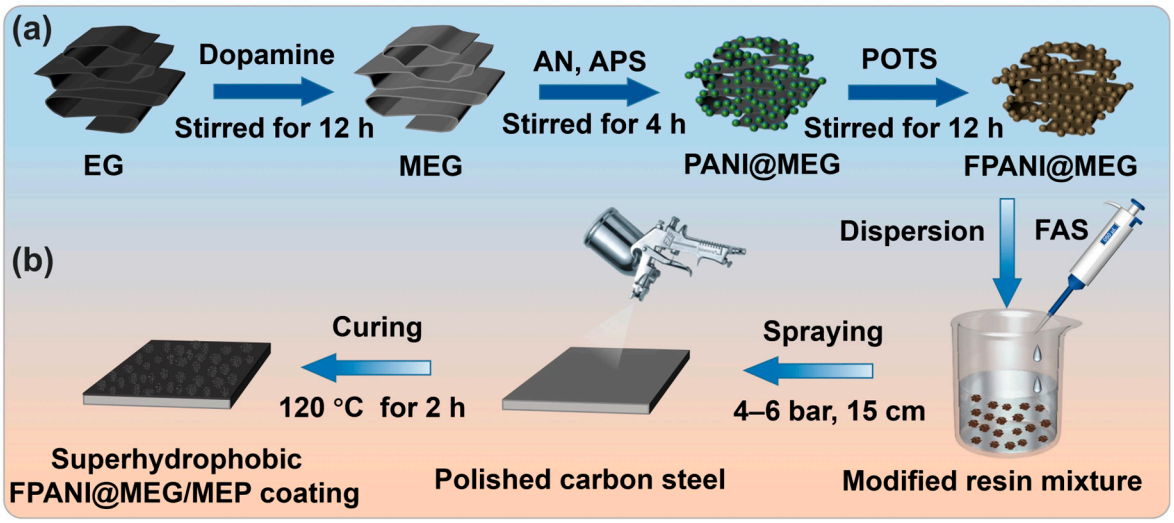

Figure 1. Schematic diagram of the preparation process for (**a**) FPANI@MEG composite particles and (**b**) FPANI@MEG/MEP superhydrophobic coating.

2.4. Fabrication of the FPANI@MEG/MEP Superhydrophobic Coating

To ensure sufficient dilution of the subsequent reaction system, 1 g of E44 epoxy resin was completely dissolved in 4 g of mixed solvent (xylene/n-butanol = 3:1, *v*/*v*). After the addition of 0.25 g of 593 curing agent, the mixture was stirred, ultrasonically dispersed for about 5 s, and then magnetically stirred for 30 min. Subsequently, 5 µL of low-surface-energy substance FAS was introduced. After uniform dispersion, magnetic stirring was continued for another 30 min to obtain the modified epoxy resin (MEP) solution. Different amounts of FPANI@MEG composite particles were added to the above MEP mixture, and the mixture was stirred and ultrasonicated simultaneously for about 2 min to achieve uniform dispersion. The resulting mixture was spray-coated onto pretreated substrates at a pressure of 4–6 bar, with a spray distance of approximately 15 cm to ensure uniform deposition. The heating stage was set at 60 °C to facilitate stable solvent evaporation from the mixture. After spraying, the sample was left to allow solvent evaporation at room temperature for 4 h, followed by curing at 120 °C in an oven for 2 h, yielding the FPANI@MEG/MEP superhydrophobic coating (Figure 1b). For comparison, FPANI/MEP and FEG/MEP coatings were also prepared using the same fluorination modification and spraying procedures.

2.5. Characterization

2.5.1. Structure and Composition Characterization

The microstructure of the composite particles and the coating surfaces was characterized by a scanning electron microscope (SEM, Zeiss SIGMA, Oberkochen, Germany). The composition changes in the epoxy resin before and after modification were analyzed by Fourier-transform infrared spectroscopy (FT-IR, PerkinElmer Spectrum 3, Waltham, MA, USA) and X-ray photoelectron spectroscopy (XPS, Thermo Fisher ESCALAB 250xi, Waltham, MA, USA). The modification and loading behavior, as well as the thermal stability changes in the prepared particles, were investigated via thermogravimetric analysis (TGA, Netzsch STA 449 F5, Selb, Bavaria, Germany) under test conditions ranging from room temperature to 800 °C in an air atmosphere with a heating rate of 10 °C/min.

2.5.2. Wettability and Adhesion Tests

The wettability of the coating surface was measured using a contact angle meter (JGW-360A, Kunshan, China) with approximately 5 μL of distilled water. At least five different positions on each sample were measured, and the average value was calculated. The sliding angle was measured by manually tilting the platform until a 5 μL droplet began to move. The tilt angle was calculated as $\theta = \arctan(\Delta h/L)$, where Δh was the vertical height difference between the two ends and L was the horizontal distance between the supporting points. Reported values were averages of at least five measurements at different positions on the same sample. The adhesion resistance of the coating to the metal substrate was evaluated according to GB/T 9286. A cross-cut tool was used to scribe a grid pattern with 2 mm spacing on the coating surface. A strong adhesive tape was repeatedly applied and rapidly peeled off until no further coating detachment occurred within the grid area. The proportion of the detached area was observed, and the corresponding grade was determined. Surface roughness (Ra) was measured using a roughness tester (Mitutoyo, SJ-210, Kawasaki, Japan) with a scanning length of 15 mm. Measurements were taken perpendicular to the coating direction across five different regions on each sample, and the average Ra value was calculated.

2.5.3. Mechanical Stability Tests

Under test conditions of a 250 g load and 1000-grit abrasive paper as the friction counterpart, the wear resistance of the composite coating was evaluated using a Taber abrasion tester in accordance with ASTM D4060-14. After every 100 abrasion cycles, the coating surface and the abrasive paper surface were cleaned by air blowing to remove loose wear debris, and the changes in mass and wettability were recorded. Mass measurements were performed using an analytical balance (Mettler Toledo, AL 104, d = 0.0001 g, Greifensee, Switzerland). The impact resistance of the coating surface structure was assessed using an LS-type falling-sand abrasion tester. Prior to testing, the coating specimen was fixed on a backing plate inclined at 45°, and 50 g of standardized fine quartz sand was released instantaneously from a height difference of 1 m. After fine particles were removed from the coating surface by air blowing, the contact angle and sliding angle were measured, marking one cycle. Each mechanical stability test was repeated at least three times per sample.

2.5.4. Environmental Adaptability Tests

The acid and alkali resistance of the coating was evaluated by measuring the change in wettability upon contact with liquid droplets of varying pH values. Weathering resistance was assessed by placing the coating in a UV aging chamber at 55 °C with an irradiance of 160 W, measuring the contact angle and sliding angle every 24 h. Antifouling performance was evaluated using a 10 wt% halloysite slurry, which was prepared by fully dispersing 10 g

of halloysite particles (particle size: 2–20 μm) in 90 mL of distilled water. The test samples were then subjected to repeated dipping-withdrawal cycles in the slurry, after which the extent of contaminant attachment on the sample surfaces was observed. Self-cleaning performance was assessed by spreading a layer of fine sand on the coating surface inclined at approximately 15° to simulate particle deposition, and observing sand residue after dropping 5 mL of methyl blue aqueous solution.

2.5.5. Corrosion Resistance Tests

The corrosion resistance of the prepared coatings was evaluated by electrochemical impedance spectroscopy (EIS) using an electrochemical workstation (PARSTAT 3000A, Oak Ridge, TN, USA). The tests were conducted in a 3.5 wt% NaCl solution using a three-electrode system, with a platinum sheet as the counter electrode, a saturated calomel electrode as the reference electrode, and the prepared coating as the working electrode. EIS was performed over a frequency range from 10^5 to 10^{-2} Hz with an amplitude of 10 mV after the open circuit potential reached a steady state. The EIS data were fitted using ZSimDemo 3.30d software, and the coating thickness was approximately 120 ± 10 μm.

3. Results and Discussion

3.1. Analysis of Epoxy Resin Modification

Upon crosslinking with amine curing agents, the cured epoxy resin coating contains polar groups such as hydroxyl and residual amino groups that can form hydrogen bonds with water, resulting in certain hydrophilicity. To reduce the risk of localized corrosion caused by hydrophilicity, fluorination modification was carried out via chemical grafting of low-surface-energy species. Hydroxyl groups generated by FAS hydrolysis underwent dehydration condensation with hydroxyl groups in the epoxy resin upon heating, achieving fluorinated modification. FT-IR was employed to characterize chemical composition changes before and after modification (Figure 2a). The appearance of Si-O stretching at 878 cm^{-1} and Si-O-C stretching at 1118 cm^{-1} and 958 cm^{-1} confirmed the grafting reaction between epoxy resin and hydrolyzed FAS. Furthermore, the XPS full spectra (Figure 2b,c) showed a remarkable increase in fluorine content in MEP. In the C1s fine spectra (Figure 2d,e), binding energies at 291.56 eV and 293.88 eV corresponded to CF_2 and CF_3 groups [29], respectively, further verifying that FAS successfully imparted low-surface-energy properties to the epoxy resin.

3.2. Morphology and Composition Analysis of Particles

The surface morphologies of EG particles after expansion, modification, and loading are presented in Figure 3. As shown in Figure 3a, EG exhibited a typical three-dimensional worm-like structure after high-temperature expansion, with irregular lamellar folds overlapping each other to form an accordion-like morphology, which was conducive to forming a physical barrier against corrosive media. In addition, defects such as cracks and pores on the EG surface provided abundant adsorption sites for the in situ self-polymerization of dopamine. As illustrated in Figure 3b, PDA was uniformly attached to the surface of the EG in the form of a thin film with a delicate network structure, forming a stable interfacial layer. On this basis, PANI was uniformly and tightly coated on the MEG surface in the form of nanoparticles, as shown in Figure 3c. This not only optimized the dispersion of PANI nanoparticles in the resin matrix but also effectively prevented the direct contact between EG particles. As an interfacial binder between EG and PANI, PDA tightly combined the two components through π-π conjugation and hydrogen bonding interactions [30,31], thereby enhancing the interfacial adhesion and structural stability of the composite particles. Furthermore, 0.1 g of powder sample was dispersed in 3 mL of mixed solvent in

a transparent vial under magnetic stirring to evaluate the dispersibility of the fillers in the coating formulation, and the results are shown in Figure 3d. After a settling time of 120 s, most of the FEG particles settled at the bottom of the vial due to their large particle size and lack of functional groups for solvent interaction. In contrast, the FPANI@MEG particles showed improved dispersibility owing to the hydrogen bonding interactions between the amino/imino groups on the PANI surface and the mixed solvent [32]. FPANI particles exhibited even slower settling because of their smaller particle size and stronger solvent interactions. Additionally, the PANI@MEG composite particles with a micro-nano hierarchical structure facilitated the construction of microstructures on superhydrophobic coating surfaces.

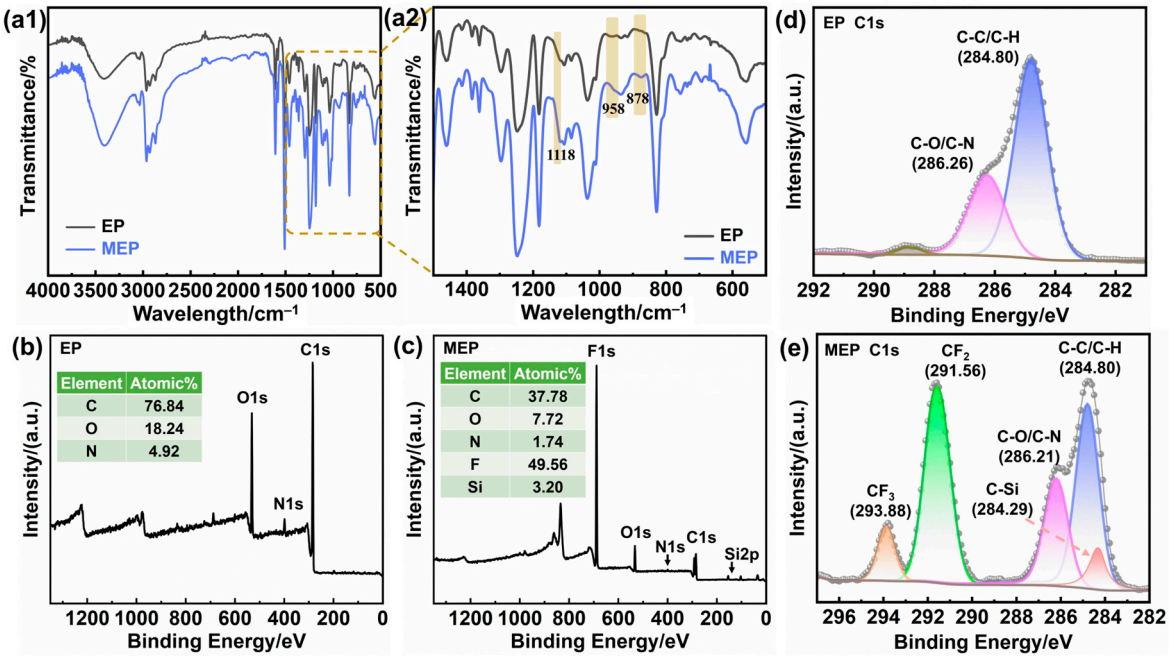

Figure 2. (**a**) FT-IR spectra, (**b**,**c**) XPS full spectra, and (**d**,**e**) C1s fine spectra of epoxy resin coating (EP) and modified epoxy resin coating (MEP).

TGA was employed to investigate the composition and thermal stability variations in the MEG and PANI@MEG particles. As shown in Figure 4a, the mass of EG began to decrease significantly around 600 °C, and its maximum decomposition rate appeared at 750 °C. In contrast, the first distinct mass loss stage of the MEG particles appeared in the range of 200–375 °C, which was attributed to the decomposition of PDA on the surface of EG, accounting for approximately 6% of the total mass. Additionally, the second mass loss stage also started at 600 °C, which corresponded to the oxidative decomposition of the remaining EG. For PANI@MEG composite particles, the first significant mass loss stage occurred before 650 °C, with a corresponding mass loss of 47.9%, which was ascribed to the decomposition of both PDA and PANI on the EG surface. Based on the proportion of PDA in MEG particles, the loading ratio of PANI was estimated to be approximately 40%. Similarly, the second mass loss stage corresponded to the oxidative decomposition of the EG. Notably, in Figure 4b, the maximum decomposition rate of EG composite particles loaded with PDA or PDA/PANI (approximately 4.0%·min^{-1}) was significantly lower than that of bare EG particles (5.2%·min^{-1}), indicating that the design of composite particles effectively reduced the decomposition rate of the materials. Furthermore, compared with EG and MEG particles, the PANI@MEG composite particles exhibited an increased initial decomposition temperature (650 °C) and a higher temperature corresponding to the maxi-

mum decomposition rate (800 °C) in the high-temperature region (>600 °C), suggesting that the loading of PANI enhanced the decomposition temperature of the material.

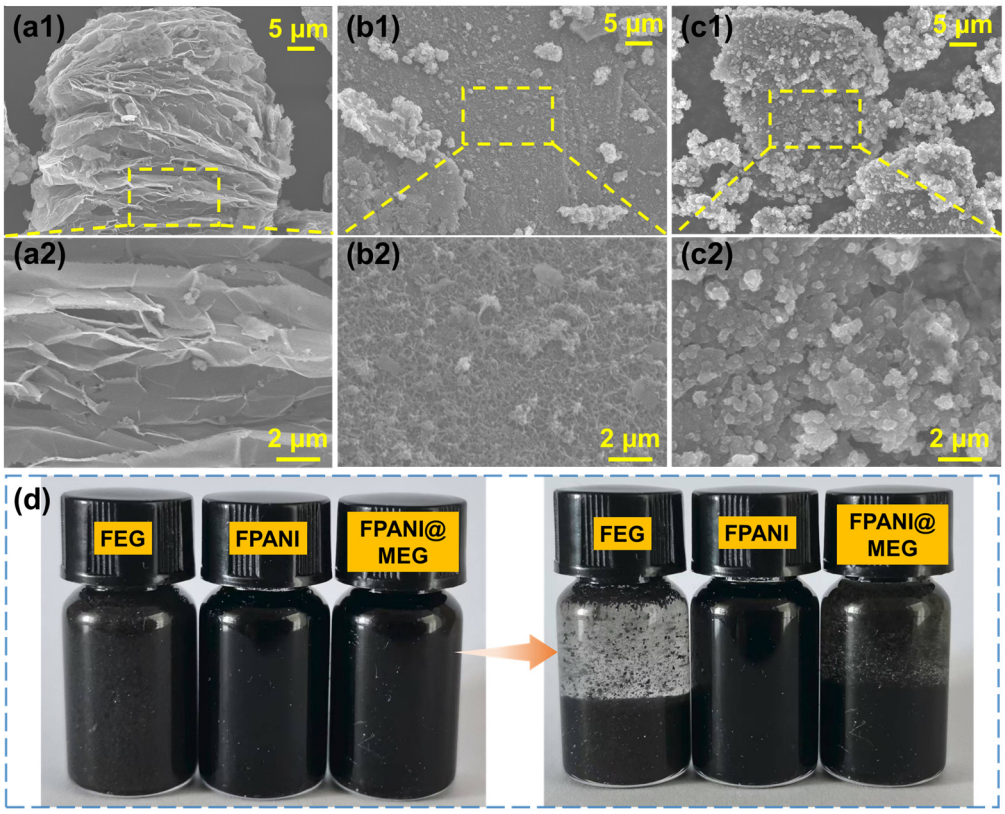

Figure 3. Surface morphology of (**a**) EG, (**b**) MEG, and (**c**) PANI@MEG composite particles; (**d**) comparison of dispersion properties of FEG, FPANI, and FPANI@MEG particles in mixed solvents used in the experiment.

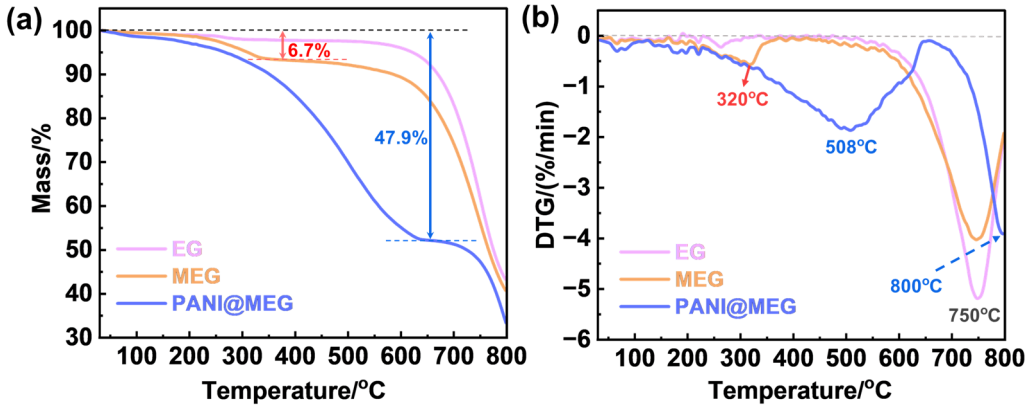

Figure 4. (**a**) TGA and (**b**) DTG curves of the EG, MEG, and PANI@MEG particles.

3.3. Surface Wettability and Morphology Analysis of Coatings

The effects of low-surface-energy substances and the additional amount of FPANI@MEG composite particles on the surface wettability of coatings were investigated using a contact angle meter, and the results are shown in Figure 5. The contact angle of the pure EP coating was 79.8 ± 1.7°, exhibiting strong hydrophilicity. In contrast, the fluorinated MEP coating exhibited significantly enhanced hydrophobicity with a contact angle of 105.4 ± 1.8°, and its reduced surface energy weakened water adsorption, thereby lowering the corrosion risk of the material. Based on the MEP coating, it was found that the contact angle and surface roughness of the coating increased with the gradual addition of FPANI@MEG particles.

However, at low particle contents (≤20 wt%), the strong encapsulation and leveling effect of epoxy resin prevented significant changes in surface morphology, resulting in slight increases in contact angle and roughness. When the particle addition reached 30 wt%, the coating contact angle was 151.9 ± 1.9°, and the sliding angle was 12.1 ± 1.0°, indicating that the surface microstructure could provide sufficient support for water droplets, while insufficient micro-nano structures led to high sliding resistance. With a further increase to 35 wt%, the contact angle reached 156.5 ± 1.8°, and the sliding angle was 3.0 ± 0.6°. The synergistic effect of abundant micro-nano structures on the coating surface (Ra = 19.95 ± 0.90 μm) and the increased low-surface-energy chemical composition contributed by the fluorinated PANI@MEG particles enabled water droplets to stably exist in the Cassie state and slide off easily, reaching the criteria for superhydrophobic surfaces. In addition, at an identical filler content of 35 wt%, the water contact angles of FEG/MEP and FPANI/MEP coatings were measured to be 144.5 ± 1.2° and 158.6 ± 0.9°, respectively.

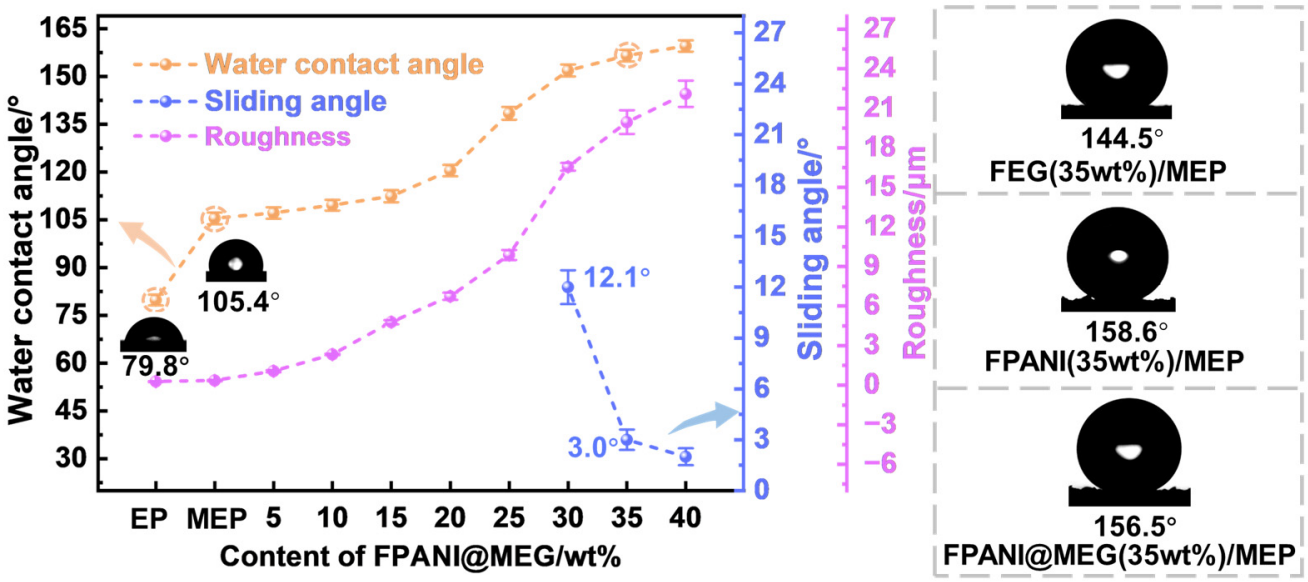

Figure 5. Surface wettability and roughness of the coating as a function of FPANI@MEG particles content.

The influence of FPANI@MEG composite particle content on the coating surface morphology was presented in Figure 6. As presented in Figure 6a, the fluorinated MEP coating without particles exhibited a smooth surface with a roughness of 0.35 ± 0.05 μm, close to 0.27 ± 0.04 μm for the pure EP coating. At the particle content of 20 wt%, local protrusions formed by particles can be observed, but most of the surface remained smooth due to the dense encapsulation by epoxy resin (Figure 6(b1)). Notably, the magnified image (Figure 6(b2)) revealed excellent interfacial compatibility between FPANI@MEG particles and the resin matrix. This stemmed from the uniform PANI coated on MEG, where hydrogen bonding between amino/imino groups and epoxy ether/hydroxyl groups, along with nanoparticle anchoring, synergistically enhanced interfacial adhesion. Such interfacial strengthening contributed to improved mechanical stability and corrosion protection of the coating. Figure 6c showed the surface morphology at 35 wt% particle loading. Micron-scale roughness combined with exposed nano-sized PANI protrusions constructed a hierarchical micro-nano structure. This structure can trap air at the solid–liquid interface to form an "air cushion", reducing the solid–liquid contact area, thereby blocking the penetration of corrosive media and prolonging the anticorrosion lifespan of the coating.

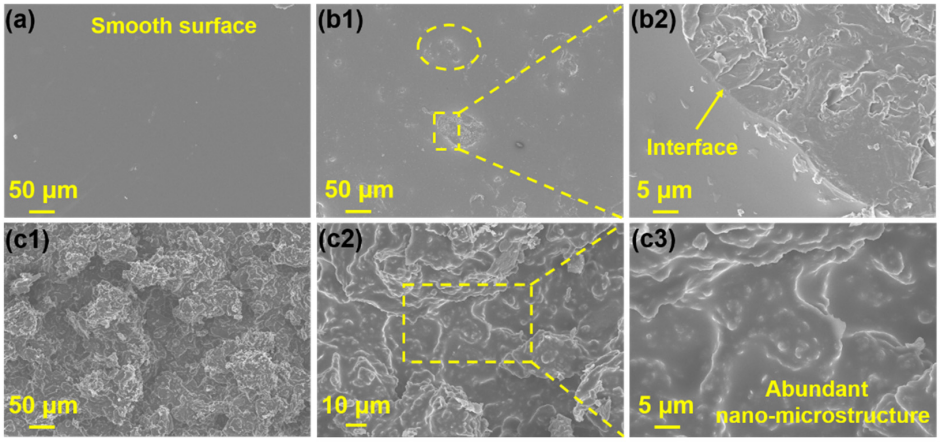

Figure 6. Surface morphology of the FPANI@MEG/MEP coating with FPANI@MEG content of (**a**) 0 wt%, (**b**) 20 wt%, and (**c**) 35 wt%.

3.4. Adhesion Analysis

The adhesion strength of the coating to the substrate directly determines its service life. According to the standard test method specified in GB/T 9286, the adhesion grades of FEG/MEP, FPANI/MEP, and FPANI@MEG/MEP coatings were evaluated. As shown in Figure 7, the FEG/MEP coating showed no peeling before or after tape stripping, with a peeling area of 0%, corresponding to Grade 0 adhesion. The FPANI/MEP coating exhibited partial flaking during cross-cutting, and the peeling area increased to 5–15% after repeated tape adhesion, corresponding to Grade 2 adhesion. For the FPANI@MEP/MEP coating, no obvious peeling occurred before and after stripping, with a peeling area < 5%, corresponding to Grade 1 adhesion. Moreover, the coating retained excellent superhydrophobicity after tape peeling. FPANI nanoparticles severely agglomerated via hydrogen bonding and π-π conjugation, hindering contact between epoxy groups and the curing agent, which reduced crosslinking density and formed a loose, porous coating with weak adhesion to the substrate [33]. In contrast, loading PANI on the MEG surface optimized the dispersion state of PANI in the resin matrix. Meanwhile, hydrogen bonding and physical anchoring effectively enhanced the interfacial bonding between composite particles and the resin, endowing the FPANI@MEG/MEP superhydrophobic coating with excellent adhesion. Furthermore, high adhesion strength contributed positively to the wear resistance of the coating and the inhibition of interfacial corrosion on the metallic substrate.

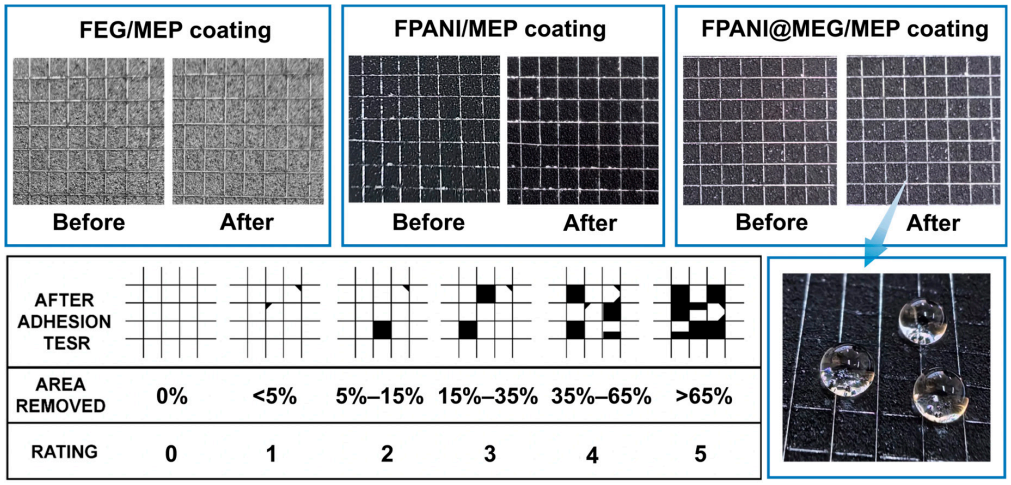

Figure 7. Digital images of the FEG/MEP, FPANI/MEP, and FPANI@MEG/MEP coatings before and after the adhesion test, along with the evaluation standard for coating adhesion rating (GB/T9286).

3.5. Mechanical Stability and Hydrophobic Durability of the Coating

During service, superhydrophobic coatings may be subjected to external damage such as abrasion or impact from hard objects, leading to varying degrees of mechanical damage, structural destruction, and the loss of surface hydrophobicity. The Taber abrasion test and falling-sand impact test were conducted to assess the structural stability and hydrophobic durability of the FPANI@MEG/MEP superhydrophobic coating.

3.5.1. Abrasion Resistance Analysis

Figure 8a presents the mass loss of FPANI/MEP, FEG/MEP, and FPANI@MEG/MEP coatings during the Taber abrasion test as a function of abrasion cycles. The results indicated that the mass loss of all three coatings gradually increased with the number of abrasion cycles, which was attributed to the micro-cutting effect of sandpaper abrasive particles on the coating surface and the continuous generation of wear debris. The final mass loss followed the order of FPANI/MEP (125.1 ± 5.1 mg), FPANI@MEG/MEP (57.4 ± 3.9 mg), and FEG/MEP (50.2 ± 2.8 mg). Figure 8b showed the wettability changes in the FPANI@MEG/MEP superhydrophobic coating. Despite suffering severe structural damage in the initial abrasion stage due to its high surface roughness (Ra = 19.95 ± 0.90 μm), as evidenced by over half of the total mass loss within the first 200 cycles, the coating maintained a contact angle above 150° until 400 abrasion cycles.

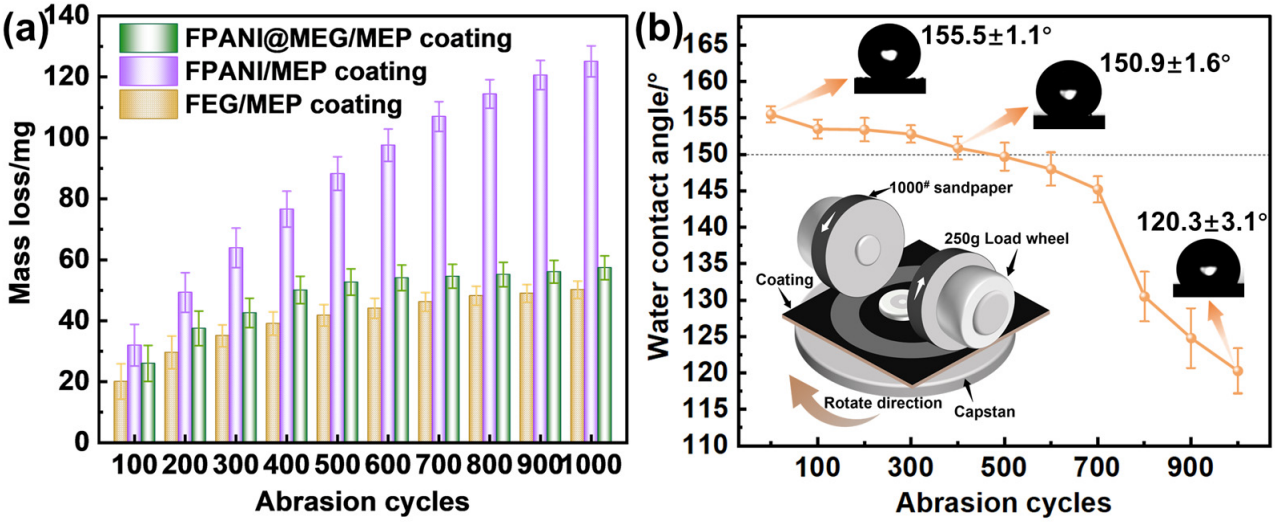

Figure 8. (**a**) Wear mass loss of the FEG/MEP, FPANI/MEP, and FPANI@MEG/MEP coatings as a function of abrasion cycles, and (**b**) the effect of abrasion cycles on the surface wettability of the FPANI@MEG/MEP superhydrophobic coating.

Figure 9 displayed the worn surface morphologies of the three coatings to reveal their distinct abrasion behaviors. For the FEG/MEP coating (Figure 9a), the incorporated EG consists of stacked graphene sheets with weak interlayer van der Waals forces. The nanosheets slid out under shear stress and formed a continuous tribolayer at the friction interface, which prevented direct contact between the friction pairs and reduced cutting damage from the sandpaper [34]. Meanwhile, the worm-like structure allowed some wear debris to be stored in micro-pits where EG resided under applied pressure, further reducing the wear loss of the coating. For the FPANI/MEP coating (Figure 9b), the loose and porous structure resulting from nanoparticle agglomeration led to continuous generation of fine debris under sandpaper abrasion. Although a small part of nanoparticles formed a tribolayer between friction pairs [35], it could not compensate for the structural looseness, resulting in the highest mass loss compared with the other coatings. For the FPANI@MEG/MEP

superhydrophobic coating, before 400 abrasion cycles, the remaining protrusions and gradually exposed underlying rough structures (Figure 9c) still retained the ability to trap air cushions, which explains why the coating maintained its superhydrophobicity during this stage. Therefore, before a continuous tribolayer formed, the mass loss mainly arose from the consumption of the hierarchical structure. Under cyclic abrasion, detached FPANI@MEG debris gradually filled surface pits and formed a composite tribolayer (Figure 9d). After 400 cycles, the mass loss rate decreased as the tribolayer coverage increased. Meanwhile, severe structural damage and loss of low-surface-energy species reduced the final contact angle to 120.3 ± 3.1°.

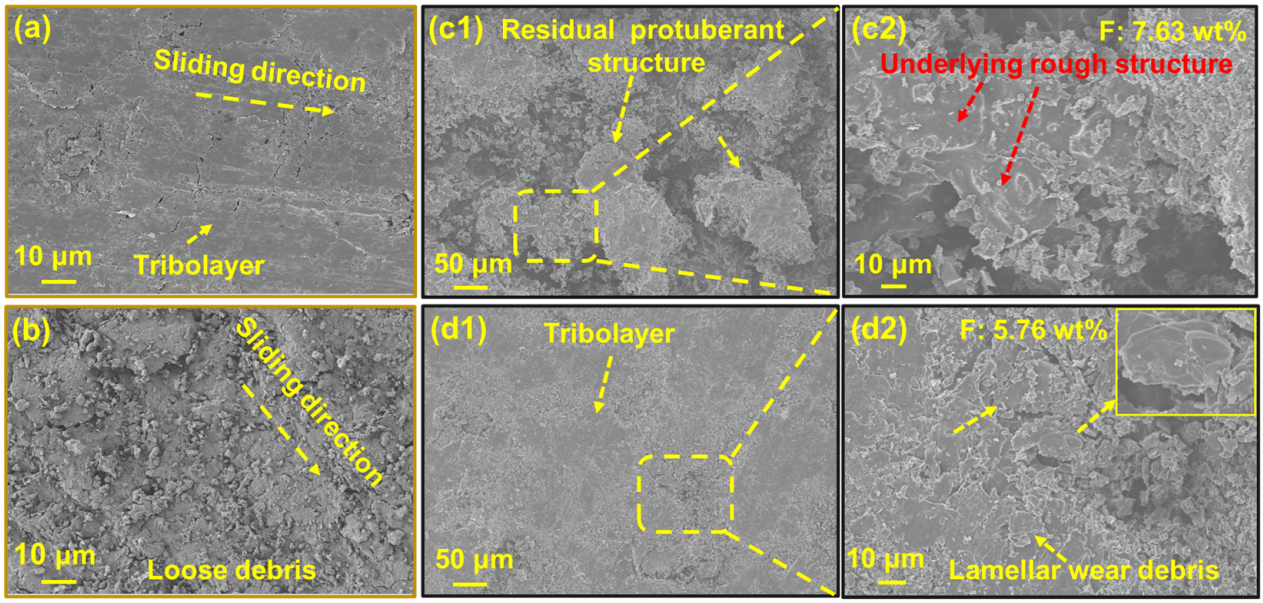

Figure 9. Worn surface morphology of (**a**) FEG/MEP and (**b**) FPANI/MEP coating after Taber abrasion test; worn surface morphology of FPANI@MEG/MEP superhydrophobic coating after (**c**) 400 and (**d**) 1000 abrasion cycles.

3.5.2. Impact Resistance Analysis

Figure 10a presents the schematic diagram of the falling-sand impact test process, along with the changes in surface wettability of the FPANI@MEG/MEP superhydrophobic coating under cyclic falling-sand impact. As the number of impact cycles increased, the contact angle of the coating gradually decreased, while the sliding angle increased. After the ninth impact, corresponding to a cumulative sand mass of 450 g, the contact angle decreased to approximately 150°, and the coating lost its superhydrophobicity after the tenth impact. Surface morphology image of the impacted area revealed that the periodic sand impact partially damaged the micro-nanoscale rough structures on the coating surface (Figure 10b), reducing its ability to trap air. Additionally, the loss of low-surface-energy substances decreased the fluorine content from 11.0 wt% to 8.6 wt%, resulting in reduced hydrophobicity. Notably, after heat treatment at 120 °C for 5 min, the contact angle recovered from 144.8° to 153.2° (Figure 10c), and a distinct silver mirror phenomenon reappeared in the tested area (Figure 10d), which indicated that the coating possessed thermal healing potential. It may be attributed to the fact that heating promoted the migration of fluorine-containing species from the coating interior to the surface, leading to a reduction in surface energy [36]. The above results demonstrated that the FPANI@MEG/MEP superhydrophobic coating exhibited good abrasion resistance, impact resistance, and hydrophobic durability.

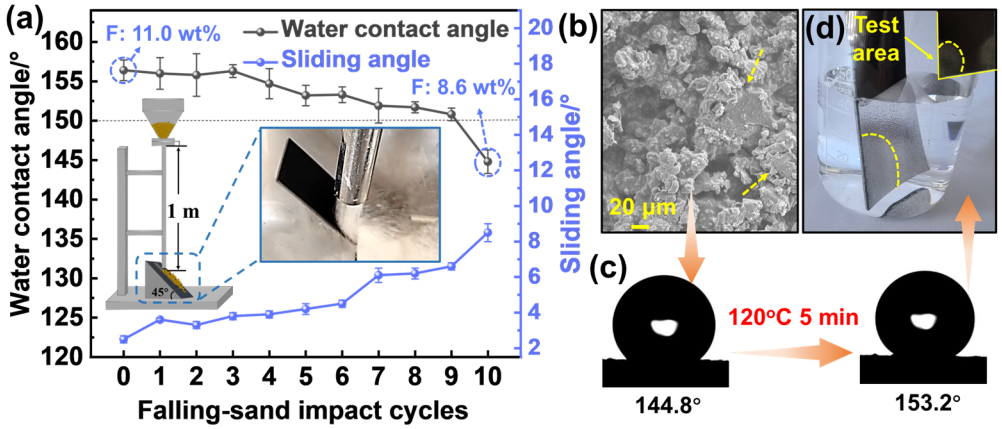

Figure 10. (**a**) Effect of falling-sand impact cycles on the surface wettability of FPANI@MEG/MEP superhydrophobic coatings (inset: schematic illustration of the falling-sand impact tester); (**b**) surface morphology of the coating after sand impact testing; (**c**) changes in contact angle before and after thermal healing; (**d**) silver mirror phenomenon observed on the thermally healed surface.

3.6. Environmental Adaptability Analysis

Acid/alkaline liquid environments or outdoor light exposure may compromise the chemical composition or surface morphology of superhydrophobic coatings, leading to changes in surface wettability. Therefore, acid/alkali resistance tests and UV aging tests were conducted on the as-prepared FPANI@MEG/MEP superhydrophobic coating to evaluate its superhydrophobic stability. Figure 11a presents the wettability of the coating upon contact with droplets at varying pH levels. The coating showed contact angles exceeding 154.1 ± 0.5° and sliding angles below 3.4 ± 0.2° within the pH range of 1–14, indicating stable acid/alkali resistance. It also exhibited universal superhydrophobicity toward diverse liquids, including milk, ink, coffee, juice, and cola. Furthermore, the coating maintained stable superhydrophobic performance after 60 days of UV exposure (Figure 11b). The outstanding weather resistance of the coating can be attributed to several factors. EG in the FPANI@MEG composite particles played a key role in microstructure construction, with its lamellar structure blocking some UV radiation [37,38]. Meanwhile, PANI loaded on EG absorbed UV light via its conjugated structure, mitigating UV-induced structural damage [39,40]. Additionally, the fluorinated coating surface possessed abundant C-F bonds with high bond energy, which resisted cleavage under UV irradiation, maintaining long-term low surface energy [41,42]. The synergy between a stable hierarchical structure and durable surface energy ensures the coating retains superhydrophobicity under prolonged UV exposure.

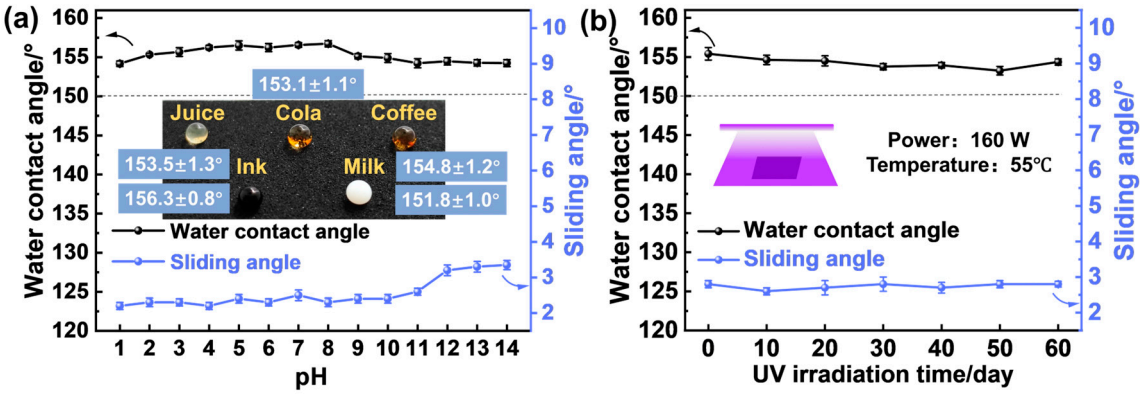

Figure 11. Effect of (**a**) acid/alkali droplet with pH value of 1–14 and (**b**) UV irradiation time on the wettability of the FPANI@MEG/MEP superhydrophobic coating.

When exposed to air or liquid environments, superhydrophobic coatings may suffer from particle deposition or contamination, where pore blockage and physical wear can damage the surface microstructure and low-surface-energy properties, thereby reducing hydrophobicity. Therefore, evaluating self-cleaning and antifouling performance is crucial for assessing their environmental suitability and practical application value. The tests were conducted using a polished substrate and the FPANI@MEG/MEP superhydrophobic coating sample as a comparison. In the self-cleaning test, methyl blue droplets on the tilted substrate surface failed to remove fine sand, showing severe retention (Figure 12a). In contrast, on the FPANI@MEG/MEP superhydrophobic coating, droplets remained spherical, rolled rapidly to the bottom, and easily carried away particles along their path without residue, leaving the surface as clean as the original state (Figure 12b), demonstrating excellent self-cleaning ability. Similarly, in the antifouling test, the substrate was heavily contaminated after just one dipping-withdrawal cycle in halloysite slurry (Figure 12c), while the superhydrophobic coating remained uncontaminated even after 30 repeated dipping-withdrawal cycles in the same slurry (Figure 12d), exhibiting outstanding anti-fouling performance. The abundant nano-micro hierarchical structure and low-surface-energy properties of the coating played a crucial role in enhancing self-cleaning and anti-fouling properties. On the one hand, test liquids only contact the protruding regions of the coating surface, while air is stably trapped within the surface cavities, making it difficult for droplets to wet the surface. Even a slight tilt allows droplets to roll off and remove surface contaminants, realizing self-cleaning. On the other hand, these surface characteristics reduce the solid–liquid contact area and lower the adhesion probability of pollutants, thereby contributing to the superior anti-fouling performance.

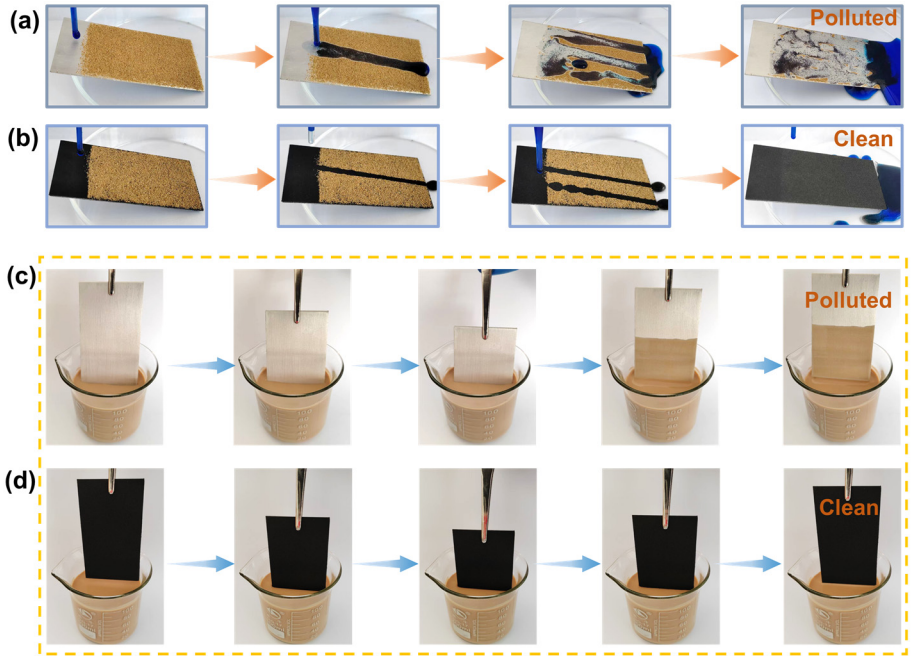

Figure 12. (**a**,**b**) Self-cleaning and (**c**,**d**) anti-fouling performance tests of the substrate and FPANI@MEG/MEP superhydrophobic coating.

3.7. Corrosion Resistance Analysis

Electrochemical data of FPANI/MEP, FEG/MEP, and FPANI@MEG/MEP coatings immersed in 3.5 wt% NaCl solution (25 °C) for various durations are presented in Figure 13. As shown in Figure 13a,c, FPANI/MEP and FPANI@MEG/MEP coatings displayed high low-frequency impedance modulus ($|Z|_{0.01Hz}$) of 8.5 × 10^7 and 3.8 × 10^7 Ω·cm^2 on the first day of immersion, respectively, accompanied by high-

frequency phase angles approaching 90°. Generally, a high $|Z|_{0.01Hz}$ value or a phase angle near 90° demonstrates good corrosion protection performance [12,43]. The excellent initial anticorrosion performance of FPANI/MEP and FPANI@MEG/MEP coatings can be primarily attributed to their superhydrophobic characteristics. A visible silver mirror effect was detected when the coatings contacted NaCl solution, confirming the existence of a stable trapped air film on the superhydrophobic surfaces. This intrinsic air film greatly reduced the actual contact area between corrosive electrolyte and coating substrate, efficiently suppressing the infiltration and diffusion of aggressive ions. Consequently, the coatings maintained strong corrosion shielding ability at the initial immersion stage. In contrast, the FEG/MEP coating (Figure 13b) showed a much lower initial $|Z|_{0.01Hz}$ of only 1.14×10^5 $\Omega \cdot cm^2$, together with a high-frequency phase angle of approximately 20°, indicating that the coating was rapidly penetrated and lost its protective capability shortly after exposure to the NaCl solution.

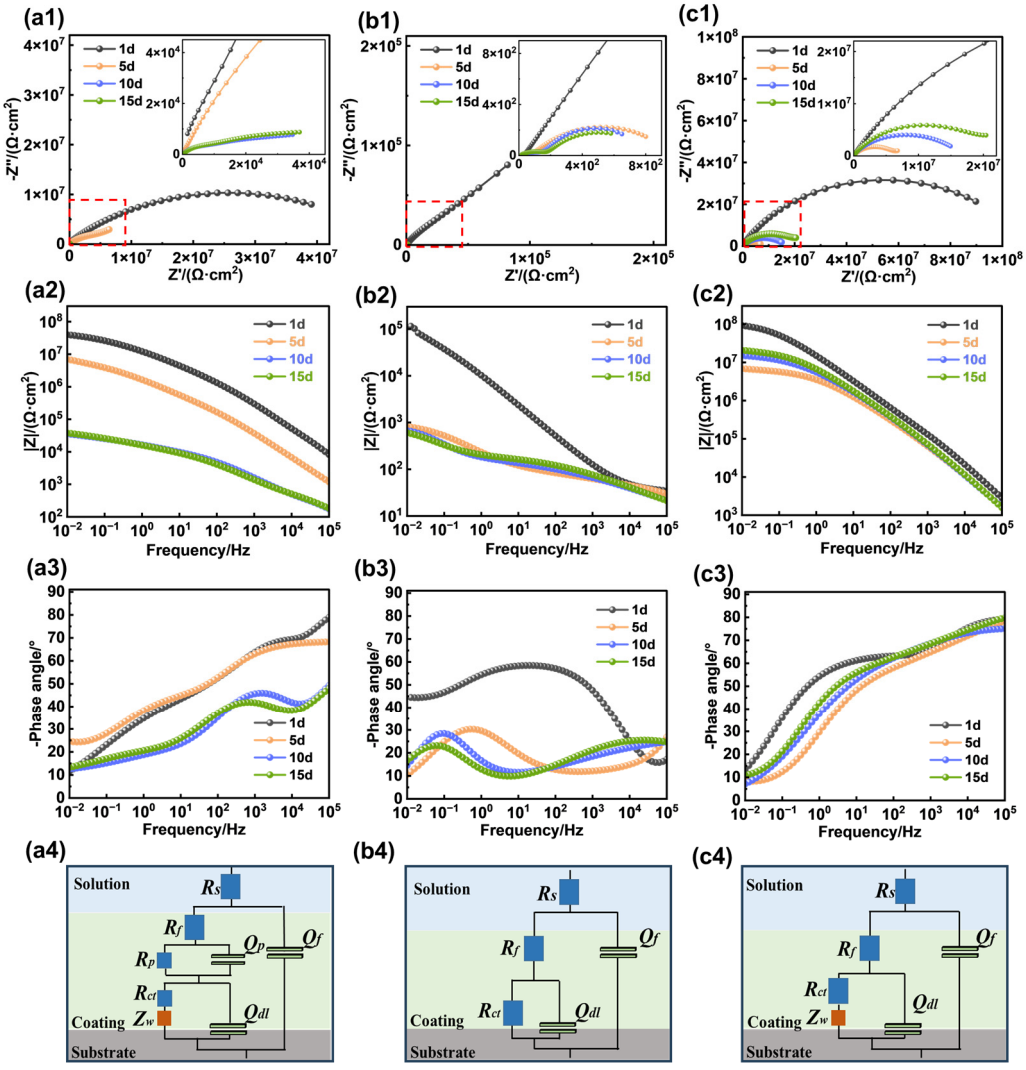

Figure 13. Nyquist plots (the first row), Bode plots (the second and third rows), and equivalent circuit models of (**a**) FPANI/MEP, (**b**) FEG/MEP, and (**c**) FPANI@MEG/MEP coatings immersed in 3.5 wt% NaCl solution (25 °C) for 15 days.

As shown in Figure 13(a2,b2), the $|Z|_{0.01Hz}$ of FPANI/MEP and FEG/MEP coatings declined markedly as immersion time extended, demonstrating the gradual deterioration and failure of their barrier protection performance toward the substrate. For FPANI/MEP coating, a loose and porous microstructure severely weakened its intrinsic barrier ability.

During continuous immersion, water and chloride ions rapidly infiltrated through internal pores and defects to reach the metal substrate, initiating substrate corrosion. Meanwhile, this rapid penetration also prevented PANI within the coating from participating in redox reactions to exert its corrosion inhibition effect. In contrast, the FEG/MEP coating displayed an even weaker barrier effect and a faster corrosion degradation process. Obvious rust observed on the coating surface after only 4 days of immersion, together with the electrolyte solution changing from colorless to light brown, confirmed the severe breakdown of coating barrier integrity. Notably, the capacitive arc of the FPANI@MEG/MEP coating initially shrank and then expanded with increasing immersion time (Figure 13(c1)), and the corresponding $|Z|_{0.01\ Hz}$ showed a trend of initial decrease followed by continuous rise (Figure 13(c2)). An obvious recovery of corrosion protection performance appeared on the 10th day of immersion, with the $|Z|_{0.01\ Hz}$ increasing from $6.80 \times 10^6\ \Omega{\cdot}cm^2$ on the 5th day to $1.45 \times 10^7\ \Omega{\cdot}cm^2$ (nearly one order of magnitude improvement), and further increasing to $2.30 \times 10^7\ \Omega{\cdot}cm^2$ by the 15th day. A more pronounced advantage in corrosion protection performance was demonstrated in Figure 14a, where the FPANI@MEG/MEP coating stood out prominently.

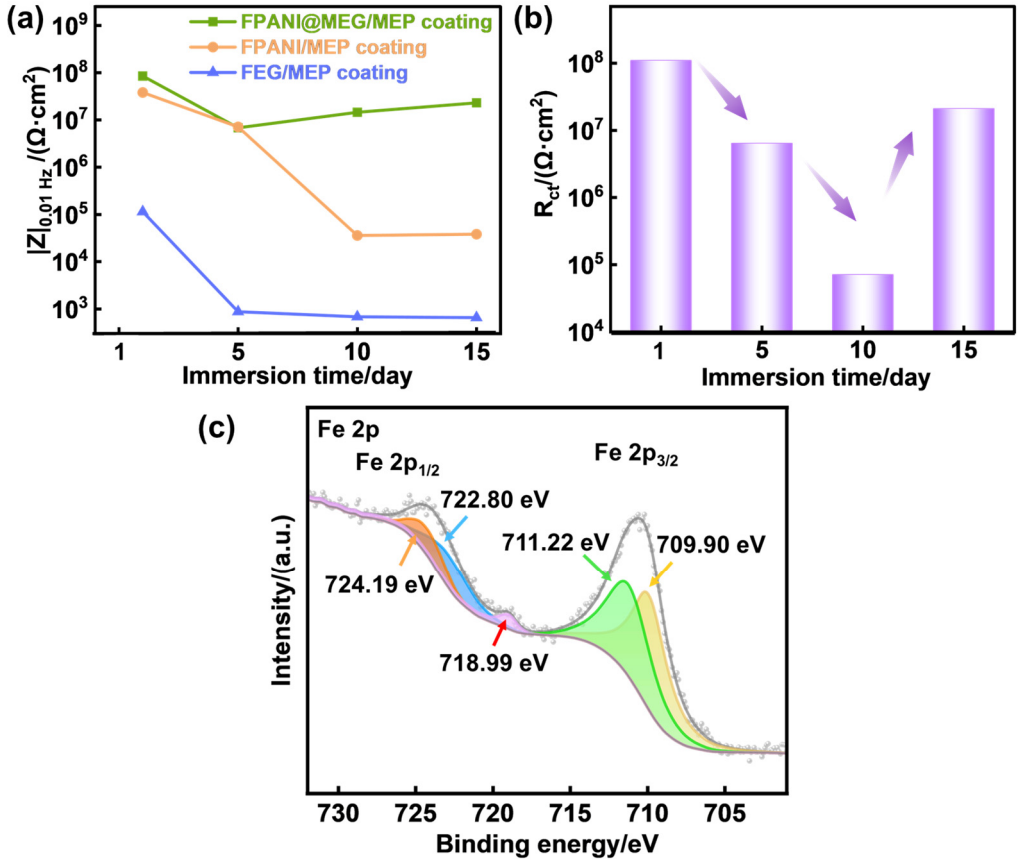

Figure 14. (**a**) Comparison of $|Z|_{0.01\ Hz}$ for FPANI@MEG/MEP, FPANI/MEP, and FEG/MEP coatings at different test time points; (**b**) variation of R_{ct} with the immersion time for FPANI@MEG/MEP coating; (**c**) Fe 2p XPS spectra of the carbon steel plate coated by FPANI@MEG/MEP coating.

The EIS spectra of the three coatings were fitted using the equivalent circuit models displayed in Figure 13(a4), (b4), and (c4), respectively, and the corresponding electrochemical fitting parameters were summarized in Table 1. In the equivalent circuit, elements R_s, R_f, R_p, R_{ct}, and Z_w correspond to the solution resistance, coating resistance, pore resistance, charge transfer resistance, and Warburg impedance, respectively. Elements Q_f, Q_p, and Q_{dl} represent constant phase elements (CPEs) [44,45]. As shown in Table 1, the FPANI@MEG/MEP

coating exhibited the highest R_{ct} at the 15th day, reaching 2.11×10^7 $\Omega \cdot cm^2$, which was significantly higher than that of the other coatings, indicating that the electrochemical corrosion reaction at the coating/substrate interface was effectively suppressed. Furthermore, the temporal evolution of R_{ct} for the FPANI@MEG/MEP coating over the 15-day immersion period was shown in Figure 14b, revealing an initial decrease followed by a subsequent increase. To further elucidate the reason for the change in charge transfer resistance, XPS analysis was performed on the substrate of the FPANI@MEG/MEP coating sample after immersion, and the Fe 2p spectrum is shown in Figure 14c. The peaks at 709.90 eV and 722.80 eV corresponded to Fe^{2+}, while those at 711.22 eV and 724.19 eV corresponded to Fe^{3+} [46,47], which were characteristic peaks of Fe_3O_4. In addition, a satellite peak belonging to γ-Fe_2O_3 was observed at 718.99 eV [48]. These results indicated that the protective film was mainly composed of γ-Fe_2O_3 and Fe_3O_4, suggesting that FPANI@MEG composite particles can form a passive film on the substrate surface, thereby enhancing the anticorrosion performance of the coating.

Table 1. The fitted electrochemical parameters for contrast coatings after immersion in 3.5 wt% NaCl solution (25 °C) for 15 days.

	Coating	FPANI/MEP	FEG/MEP	FPANI@MEG/MEP
	R_s ($\Omega \cdot cm^2$)	4.81×10^{-5}	4.96	1.32×10^{-4}
Q_f	Y_0 ($\Omega^{-1} \cdot cm^2 \cdot s^n$)	3.15×10^{-5}	3.33×10^{-4}	3.56×10^{-8}
	n_1	0.10	0.38	0.62
	R_f ($\Omega \cdot cm^2$)	5.06×10^{-5}	198.5	4688
Q_P	Y_0 ($\Omega^{-1} \cdot cm^2 \cdot s^n$)	6.89×10^{-7}	/	/
	n_1	0.69	/	/
	R_p ($\Omega \cdot cm^2$)	297	/	/
Q_{dl}	Y_0 ($\Omega^{-1} \cdot cm^2 \cdot s^n$)	3.28×10^{-6}	5.96×10^{-3}	1.61×10^{-9}
	n_1	0.62	0.66	0.95
	R_{ct} ($\Omega \cdot cm^2$)	2.61×10^4	647.4	2.11×10^7
	Z_w ($\Omega \cdot cm^2$)	1.10×10^{-5}	/	1.60×10^{-6}

Figure 15a illustrates the schematic diagram of the corrosion protection mechanism for the FEG/MEP coating. First, the scarce surface functional groups of EG particles limited their interaction with the epoxy resin, resulting in poor interfacial compatibility, and the numerous interfacial defects facilitated rapid penetration of corrosive media. Then, the poor dispersion of EG particles led to their settling at the bottom of the coating during preparation, where they interconnected to form a conductive network. In the presence of corrosive media, these networks induce micro-galvanic corrosion on the metal substrate surface, thereby accelerating the metal corrosion rate [49,50]. In contrast, the FPANI@MEG/MEP superhydrophobic coating (Figure 15b) formed a stable air film upon initial contact with the saline medium, delaying the ingress of corrosive species. Additionally, the FPANI@MEG filler enhanced dispersion and interfacial compatibility within the resin matrix, creating a tortuous permeation pathway that improved the barrier property. Finally, electrons lost during anodic oxidation reduced the doped PANI to its reduced state. Under effective barrier conditions, iron ions preferentially reacted with oxygen to form a dense passive film [47]. Meanwhile, the conductive EG carrier facilitated electron transfer within the filler [45], promoting PANI participation and accelerating passive film formation, thereby effectively suppressing anodic dissolution. Thus, through the synergistic action of multiple protective mechanisms of air film shielding, interfacial reinforcement, physical barrier, and

anodic passivation, the FPANI@MEG/MEP superhydrophobic coating achieved superior anticorrosion performance.

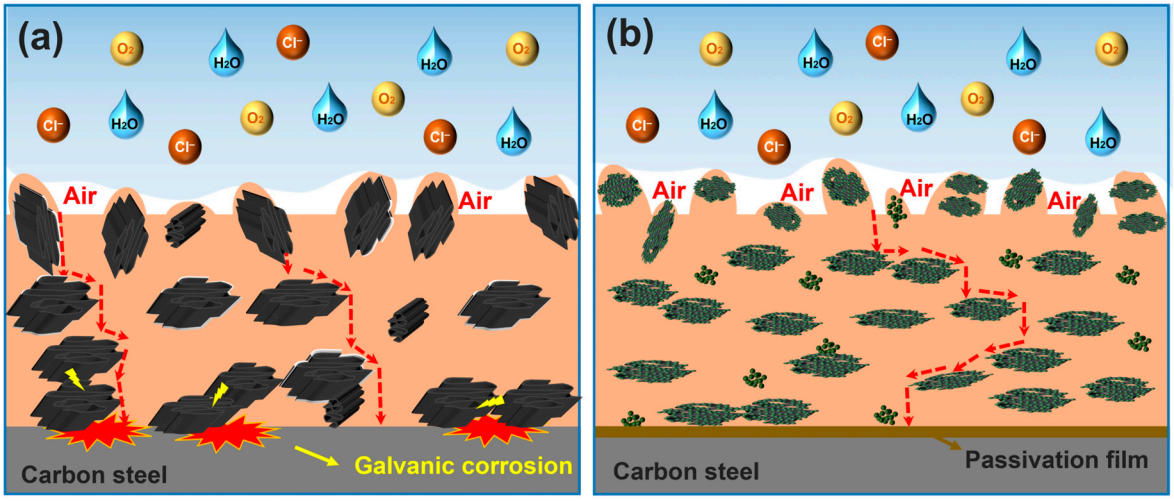

Figure 15. Schematic diagram of the corrosion protection mechanism for (**a**) FEG/MEP and (**b**) FPANI@MEG/MEP coatings.

4. Conclusions

In this work, FPANI@MEG/MEP superhydrophobic coating with good anticorrosion performance was successfully fabricated by integrating FPANI@MEG multifunctional particles with FAS-modified epoxy matrix. Strong interfacial loading between PANI and EG was achieved through in situ polymerization, leveraging the π-π conjugation/hydrogen bonding interactions formed between PDA and EG/PANI. The resulting filler plays multiple roles in coating, including constructing a micro-nano hierarchical structure, providing physical barrier effects, and enabling active passivation. The structural stability and physical shielding properties of the coating were enhanced by hydrogen bonding between the amino/imino groups on the composite particles and the epoxy ether/hydroxyl groups, as well as physical anchoring between the nanoparticles and the resin. Experimental results showed that the hydrophobicity of the fluorinated epoxy coating was significantly improved, with the water contact angle increasing from 79.8 ± 1.7° for the pure EP coating to 105.4 ± 1.8°. A superhydrophobic surface was achieved at a FPANI@MEG loading of 35 wt%, exhibiting a water contact angle of 156.5 ± 1.8° and a sliding angle of 3.0 ± 0.6°. The coating maintained its superhydrophobicity after 400 Taber abrasion cycles and 450 g of falling-sand impact, while demonstrating Grade 1 adhesion strength and applicability under various complex environments. Moreover, owing to the multiple anticorrosion mechanisms involving air film shielding, physical barrier, and metal surface passivation, the coating exhibited excellent anticorrosion performance with a $|Z|_{0.01\ Hz}$ of $2.30 \times 10^7\ \Omega \cdot cm^2$ after 15 days of immersion in 3.5% NaCl solution. A significant increasing trend in charge transfer resistance during immersion indicated that the anodic dissolution of the metal surface was effectively suppressed. Despite the remaining scope for optimization in this study, the results are expected to provide a useful reference for improving the anticorrosion performance of epoxy-based superhydrophobic coatings.

Author Contributions: M.L.: Conceptualization, Data curation, Formal analysis, Investigation, Methodology, and Writing—original draft. Y.F.: Supervision and Validation. C.W. and Y.C.: Methodology and Formal analysis. X.Z. and H.L.: Conceptualization and Methodology. Z.L.: Conceptualization, Methodology, Funding acquisition, and Writing—review and editing. H.W.: Conceptualization,

Funding acquisition, Project administration, and Writing—review and editing. All authors have read and agreed to the published version of the manuscript.

Funding: The research was financially supported by the Heilongjiang Provincial Natural Science Foundation for Excellent Youth Fund (YQ2024E007).

Institutional Review Board Statement: Not applicable.

Informed Consent Statement: Not applicable.

Data Availability Statement: The original contributions presented in this study are included in the article. Further inquiries can be directed to the corresponding authors.

Conflicts of Interest: The authors declare no conflicts of interest.

References

1. Guo, F.; Li, H.; Ma, J.; Yin, H.; Luo, H. Triple-synergistic anti-corrosion nanocapsules: Empowering coatings with outstanding corrosion resistance. *Prog. Org. Coat.* **2025**, *204*, 109254. [CrossRef]
2. Diraki, A.; Omanovic, S. Anticorrosive properties of the double-layer PANI-(graphene oxide)/epoxy coating in protecting carbon steel in saltwater. *J. Coat. Technol. Res.* **2023**, *20*, 995–1006. [CrossRef]
3. Dhongde, N.R.; Adhikari, S.; Rajaraman, P.V. Anticorrosion properties of ionic liquid functionalized graphene oxide epoxy composite coating on the carbon steel for CCUS environment. *Environ. Sci. Pollut. Res.* **2025**, *32*, 4511–4522. [CrossRef]
4. Liu, Y.; Liu, M.; Lu, X.; Wang, Z. Effect of temperature and ultraviolet radiation on corrosion behavior of carbon steel in high humidity tropical marine atmosphere. *Mater. Chem. Phys.* **2022**, *277*, 124962. [CrossRef]
5. Li, M.; Gross, A.; Taylor, B.; Zhang, H.; Liu, J. Effects of Cl-ion and temperature variations on steel corrosion in supercritical CO2 saturated aqueous environments. *Process Saf. Environ. Prot.* **2024**, *187*, 1446–1453. [CrossRef]
6. Guo, Q.; Wu, Z.; Xing, Y.; Lu, Y.; Zhang, F.; Li, W. Corrosion evolution and mechanical property deterioration of Q355NH weathering steel in long-term neutral salt spray environment. *Constr. Build. Mater.* **2024**, *411*, 134193. [CrossRef]
7. Zhao, Q.Y.; Zhao, W.J.; Wu, Y.H. Constructing bi-functional Ce-MOF on carbon fiber endowing epoxy coating with excellent anti-corrosion and erosion wear resistance. *Carbon* **2023**, *214*, 118374. [CrossRef]
8. Pessoa, M.O.; Freitas, B.R.; de Oliveira Braga, J.; Santos, S.L.B.S.; da Silva, B.P.; Capelossi, V.R.; Cotting, F. Anticorrosion and adhesion performance of a monolayer and double layer silane-epoxy coating systems applied on carbon steel. *Surf. Coat. Technol.* **2024**, *485*, 130909. [CrossRef]
9. Verma, A.; Bandyopadhyay, R.; Tiwary, C.S.; Das, B.K.; Bhattacharya, J. Engineering defect concentration and morphology of green graphene for the development of hard and anticorrosive coating on carbon steel. *Corros. Sci.* **2023**, *224*, 111523. [CrossRef]
10. Ning, Y.; Song, Y.; Li, S.; Wu, S.; Wang, Q.; Tian, H.; Liu, B. Nanocontainers with synergetic inhibition and corrosion protection abilities towards intelligent self-healing coatings. *Corros. Sci.* **2024**, *226*, 111661. [CrossRef]
11. Kumar, A.; Das, C. Anticorrosive Behavior of a Novel Ternary RGO–ZnO–PANI Nanocomposite-Reinforced Epoxy Coating on Mild Steel in Marine Environment. *Adv. Eng. Mater.* **2025**, *27*, 2500949. [CrossRef]
12. Zhang, M.; Xu, F.; Lin, D.; Peng, J.; Zhu, Y.; Wang, H. A smart anti-corrosion coating based on triple functional fillers. *Chem. Eng. J.* **2022**, *446*, 137078. [CrossRef]
13. Huang, J.-q.; Liu, K.; Song, X.; Zheng, G.; Chen, Q.; Sun, J.; Jin, H.; Jiang, L.; Jiang, Y.; Zhang, Y. Incorporation of Al_2O_3, GO, and Al_2O_3@ GO nanoparticles into water-borne epoxy coatings: Abrasion and corrosion resistance. *RSC Adv.* **2022**, *12*, 24804–24820. [CrossRef] [PubMed]
14. Li, R.; Li, M.; Wu, X.; Yu, H.; Jin, R.; Liang, J. A pine needle-like superhydrophobic Zn/ZnO coating with excellent mechanochemical robustness and corrosion resistance. *Mater. Des.* **2023**, *225*, 111583. [CrossRef]
15. Shi, L.; Yan, H.; Zhao, S.; Zhang, L.; Fan, X. A durable superhydrophobic composite coating towards superior anticorrosion/wear properties. *Appl. Surf. Sci.* **2024**, *655*, 159662. [CrossRef]
16. Xue, X.; Liang, G.; Zhang, B. Superhydrophobic anti-corrosion coating: Advancing research from laboratory to real marine corrosion environment. *Prog. Org. Coat.* **2025**, *200*, 109020. [CrossRef]
17. Li, X.; Wang, Y.; Yao, S.; Li, S. Robust superhydrophobic coatings with multi-scale micro/nano structures for long-term corrosion protection of steel structures. *Chem. Eng. J.* **2026**, *531*, 173810. [CrossRef]
18. Zhou, C.; Chen, Q.; Zhao, J.; Wang, S.; Li, J.; Ai, L.; Li, T.; Hu, C. Superhydrophobic epoxy resin coating with composite nanostructures for metal protection. *Mater. Today Commun.* **2024**, *38*, 107803. [CrossRef]
19. Li, M.L.; Wang, H.Y.; Fu, Y.X.; Jing, J.; Zhang, X.G.; Wang, C.J.; Wang, R.T.; Liu, Z.J. Fabrication of robust superhydrophobic epoxy/PANI@ CNTs coatings with excellent anti-corrosion property. *Prog. Org. Coat.* **2025**, *206*, 109373. [CrossRef]

20. Dandan Doganci, M.; Sevinç, H. Investigation of superhydrophobic and anticorrosive epoxy films with Al_2O_3 nanoparticles on different surfaces. *ACS Omega* **2023**, *8*, 21559–21570. [CrossRef]
21. Yang, H.; Dong, Y.; Li, X.; Gao, Y.; He, W.; Liu, Y.; Mu, X.; Zhao, Y.; Fu, W.; Wang, X. Development of a mechanically robust superhydrophobic anti-corrosion coating using micro-hBN/nano-Al_2O_3 with multifunctional properties. *Ceram. Int.* **2025**, *51*, 491–505. [CrossRef]
22. Zhang, W.; Liu, X.; Zheng, C.; Zhang, B. Anti-corrosion, anti-icing, and mechanically robust superhydrophobic coating based on Kaolin particles. *Colloids Surf. A Physicochem. Eng. Asp.* **2025**, *713*, 136504. [CrossRef]
23. Ding, X.; Wang, Q.; Xu, X.; Nie, X.; Xu, X.; Li, J. A novel epoxy resin composite coating containing polyaniline modified GO with triple anti-corrosion effects of barrier, passivation and corrosion inhibition. *Prog. Org. Coat.* **2024**, *194*, 108564. [CrossRef]
24. Alipour, F.; Gharieh, A.; Behzadnasab, M.; Omidvar, A. Eco-friendly AMPS-doped polyaniline/urethane-methacrylate coating as a corrosion protection coating: Electrochemical, surface, theoretical, and thermodynamic studies. *Langmuir* **2023**, *39*, 5115–5128. [CrossRef] [PubMed]
25. Fan, W.; Wang, H.; Wang, C.; Liu, Z.; Li, K.; Zhu, Y. A sustainable dynamic redox reaction passive film for long-term anti-corrosion of carbon steel surface. *J. Colloid Interface Sci.* **2020**, *580*, 146–159. [CrossRef]
26. Gašparac, R.; Martin, C.R. Investigations of the mechanism of corrosion inhibition by polyaniline. Polyaniline-coated stainless steel in sulfuric acid solution. *J. Electrochem. Soc.* **2001**, *148*, B138. [CrossRef]
27. Mourya, P.; Goswami, R.N.; Saini, R.; Ray, A.; Khatri, O.P. Epoxy coating reinforced with graphene-PANI nanocomposites for enhancement of corrosion-resistance performance of mild steel in saline water. *Colloids Surf. A Physicochem. Eng. Asp.* **2024**, *687*, 133500.
28. Wu, S.-W.; Jiang, Q.-T.; Yuan, S.; Zhao, Q.-K.; Liu, C.; Tang, H.; Sun, Q.; Duan, J.-Z.; Hou, B.-R. Environmentally friendly expanded graphite-doped ZnO superhydrophobic coating with good corrosion resistance in marine environment. *Rare Met.* **2023**, *42*, 3075–3087. [CrossRef]
29. Butoi, C.I.; Mackie, N.M.; Gamble, L.J.; Castner, D.G.; Barnd, J.; Miller, A.M.; Fisher, E.R. Deposition of highly ordered CF2-rich films using continuous wave and pulsed hexafluoropropylene oxide plasmas. *Chem. Mater.* **2000**, *12*, 2014–2024. [CrossRef]
30. Chen, X.; Zhou, J.; Zhang, Y.; Zhu, S.; Tian, X.; Meng, F.; Cui, L.; Xue, P.; Huang, R.; Sun, J. Polydopamine-modified polyaniline/nanodiamond ternary hybrids with brain fold-like surface for enhanced dual band electromagnetic absorption. *ACS Appl. Polym. Mater.* **2019**, *1*, 405–413. [CrossRef]
31. Wang, Y.; Wu, S.; Yin, Q.; Du, K.; Yin, Q.; Jiang, B.; Mo, S. Novel hybrid p-and n-type organic thermoelectric materials based on mussel-inspired polydopamine. *ACS Appl. Mater. Interfaces* **2021**, *13*, 23970–23982. [CrossRef]
32. Mora, A.-S.; Tayouo, R.; Boutevin, B.; David, G.; Caillol, S. A perspective approach on the amine reactivity and the hydrogen bonds effect on epoxy-amine systems. *Eur. Polym. J.* **2020**, *123*, 109460. [CrossRef]
33. Gao, F.; Mu, J.; Bi, Z.; Wang, S.; Li, Z. Recent advances of polyaniline composites in anticorrosive coatings: A review. *Prog. Org. Coat.* **2021**, *151*, 106071. [CrossRef]
34. Somberg, J.; Gonçalves, G.; Emami, N. Graphene oxide versus graphite and chemically expanded graphite as solid lubricant in ultrahigh molecular weight polyethylene composites. *Tribol. Int.* **2023**, *187*, 108643. [CrossRef]
35. Cao, Z.; Xia, Y. Corrosion resistance and tribological characteristics of polyaniline as lubricating additive in grease. *J. Tribol.* **2017**, *139*, 061801. [CrossRef]
36. Zheng, X.; Pang, A.-M.; Wang, Y.; Wang, W.; Bai, Y. Fabrication of UV-curable fluorosilicone coatings with impressive hydrophobicity and solvent resistance. *Prog. Org. Coat.* **2020**, *144*, 105633. [CrossRef]
37. Attia, N.F.; Park, J.; Oh, H. Facile tool for green synthesis of graphene sheets and their smart free-standing UV protective film. *Appl. Surf. Sci.* **2018**, *458*, 425–430. [CrossRef]
38. Xie, S.; Zhao, J.; Zhang, B.; Wang, Z.; Ma, H.; Yu, C.; Yu, M.; Li, L.; Li, J. Graphene oxide transparent hybrid film and its ultraviolet shielding property. *ACS Appl. Mater. Interfaces* **2015**, *7*, 17558–17564. [CrossRef] [PubMed]
39. Wang, L.; Zhou, M.; Fu, H. An in-situ growth Fe3O4 and polyaniline on carbon cloth encapsulated composite phase change materials with high thermal conductivity and photothermal energy conversion and storage. *J. Energy Storage* **2024**, *78*, 110090. [CrossRef]
40. Sharma, A.; Goyal, P.K.; Rawal, I.; Rajpal, A.; Khokhar, A.; Kumar, V.; Dahiya, S. Structural characteristics and opto-electrical properties of in-situ synthesized polyaniline films. *Opt. Mater.* **2022**, *131*, 112712. [CrossRef]
41. Liu, Z.; Zhang, C.; Zhang, X.; Wang, C.; Liu, F.; Yuan, R.; Wang, H. Durable superhydrophobic PVDF/FEVE/GO@ TiO_2 composite coating with excellent anti-scaling and UV resistance properties. *Chem. Eng. J.* **2021**, *411*, 128632. [CrossRef]
42. Griffini, G.; Bella, F.; Nisic, F.; Dragonetti, C.; Roberto, D.; Levi, M.; Bongiovanni, R.; Turri, S. Multifunctional luminescent down-shifting fluoropolymer coatings: A straightforward strategy to improve the UV-light harvesting ability and long-term outdoor stability of organic dye-sensitized solar cells. *Adv. Energy Mater.* **2015**, *5*, 1401312. [CrossRef]

43. An, K.; Sui, Y.; Wang, Y.; Qing, Y.; Long, C.; Liu, X.; Shang, Y.; Liu, C. Synergistic control of wetting resistance and corrosion inhibition by cerium to enhance corrosion resistance of superhydrophobic coating. *Colloids Surf. A Physicochem. Eng. Asp.* **2022**, *653*, 129874. [CrossRef]
44. Liang, G.; Zhou, Y.; Hai, C.; Zhang, B. Epoxy-based superhydrophobic coating with corrosion resistance, delayed icing, self-cleaning, and substrate applicability. *Mater. Today Commun.* **2025**, *44*, 112143. [CrossRef]
45. Wang, G.; Meng, F.; Zhu, S.; Wang, F.; Liu, L. Enhancement of the shielding/passivation dual functions of PANI-SSA/epoxy composite coatings by rGO for long-term anti-corrosion of Al alloy. *Compos. Commun.* **2025**, *55*, 102302.
46. Li, C.; Li, Y.; Wang, X.; Yuan, S.; Lin, D.; Zhu, Y.; Wang, H. Synthesis of hydrophobic fluoro-substituted polyaniline filler for the long-term anti-corrosion performance enhancement of epoxy coatings. *Corros. Sci.* **2021**, *178*, 109094. [CrossRef]
47. Fan, W.; Wang, H.; Wang, C.; Liu, Z.; Wang, Z.; Liu, S.; Zhu, Y. Oxygen vacancy modified α-Fe2O3 nanorods provide an environment-friendly and efficient anti-corrosion passive film into polymer coating. *Corros. Sci.* **2023**, *215*, 111045. [CrossRef]
48. Yamashita, T.; Hayes, P. Analysis of XPS spectra of Fe2+ and Fe3+ ions in oxide materials. *Appl. Surf. Sci.* **2008**, *254*, 2441–2449. [CrossRef]
49. Dutta, D.; Ganda, A.N.F.; Chih, J.-K.; Huang, C.-C.; Tseng, C.-J.; Su, C.-Y. Revisiting graphene–polymer nanocomposite for enhancing anticorrosion performance: A new insight into interface chemistry and diffusion model. *Nanoscale* **2018**, *10*, 12612–12624. [CrossRef]
50. Kumar, S.S.A.; Bashir, S.; Ramesh, K.; Ramesh, S. New perspectives on graphene/graphene oxide based polymer nanocomposites for corrosion applications: The relevance of the graphene/polymer barrier coatings. *Prog. Org. Coat.* **2021**, *154*, 106215. [CrossRef]